Experimental and FEM study of surface modification of nickel-based superalloy subjected to ultrasonic surface rolling process

Weiwei Yu
Jie Wu
Yugang Li
Qinglong An
Weiwei Ming
Dong Chen
Haowei Wang
Ming Chen (mchen@sjtu.edu.cn)

Research Article

Keywords: Ultrasonic surface rolling process, Mechanical properties, Surface layer, GH4169 superalloy, Finite element model

Posted Date: February 21st, 2023

DOI: https://doi.org/10.21203/rs.3.rs-2598290/v1

Version of Record: A version of this preprint was published at The International Journal of Advanced Manufacturing Technology on September 30th, 2023. See the published version at https://doi.org/10.1007/s00170-023-12299-9.

Abstract

GH4169 superalloy is widely used in the manufacture of key components such as high-pressure turbine disks, turbine blades and combustion chambers of gas turbines and aero-engines. However, mechanical and metallurgical properties of the surface layer have changed significantly on account of the cutting process, which is easy to cause fatigue failure. Therefore, surface strengthening of GH4169 superalloy subjected to ultrasonic surface rolling process (USRP) is investigated, involved with the mechanical properties and microstructure of the surface layer. The findings demonstrate that the USRP treatment reduces the surface roughness of the basis sample by 93% (from 1.17 μm to 0.08 μm). The USRP treatments improve the degree of the grain refinement, the number proportion of low angle grain boundaries and dislocation density. The depth of residual compressive stress layer and hardened layer of the samples subjected to USRP treatment are improved to 0.6 mm. Moreover, finite element models are utilized to aid in the research of the USRP treatment, especially the stress and strain fields.

1 Introduction

GH4169 superalloy the Ni-Cr-Fe-based deformed alloy created in the 1950s by the United States. GH4169 superalloy still has excellent comprehensive properties under high temperature conditions, such as resistance to fatigue, corrosion, and creep [1, 2]. Therefore, GH4169 superalloy is widely used in the manufacture of key components such as high-pressure turbine disks, turbine blades and combustion chambers of gas turbines and aero-engines [3].

To enhance the resistance to fatigue, the surface strengthening process is usually used as the last step in the manufacture of parts. Investigations have indicated that forming gradient nanostructures on the surface layer via surface plastic deformation (SPD) is a crucial method to improve the fatigue properties and surface wear resistance [4, 5]. Currently, there are several approaches to generate gradient nanostructures, including mechanical shot peening (SP) [6, 7], surface mechanical grinding treatment (SMAT) [8, 9], surface mechanical rolling treatment (SMRT) [10, 11], deep rolling processing (DP) [12, 13], and laser shock strengthening (LSP) [14, 15], etc. Messé et al. [16] researched the effect of SP on the surface layer microstructure of RR1000. The results indicated that the plastic deformation generating by SP induces the diffusion of dislocations in different planes, and the dislocation density increased as the distance of SP increases. Nagarajan et al. [17] investigated the effect of rolling process on the microstructure, work hardening and residual stress (RS) of IN100 and RR1000 nickel-based superalloys. The study found that the original coarse grains (> 200 μm) of the surface layer of the IN100 specimen were compressed to a size of 40 μm ~ 50 μm after rolling process, which was obvious grain refinement. Since the grains of the RR1000 sample itself were very fine, the dislocation motion during the deformation process was intercepted by the grain boundaries. Rolling process caused work hardening, with a 50% increase in hardness of IN100 and only a 10% increase in hardness of RR1000.

At present, ultrasonic technology has been employed in the surface strengthening process, which has attracted the attention of many researchers. After ultrasonic shot peening (USP) of Inconel 718 for

different times of 45, 60 and 90 min, Kumar et al. [18] employed x-ray diffraction (X-ray), scanning electron microscope (SEM) and transmission electron microscope (TEM) to inspect the surface layer microstructure of the USP specimen. The study found that the surface layer possessed a nanostructure with a depth of about 90 μm and a grain size of about 25 nm to 40 nm. As the peening time increased, the nanograin size decreased and the δ phase was elongated. The surface microhardness rose by roughly 20%.

Different from other surface strengthening processes, USRP combines the advantages of both traditional rolling [19] and ultrasonic impact [20] technologies. USRP can not only squeeze and strengthen the surface of the material during processing, but also cause dynamic impact on the surface. When the balls impact the surface of the sample at high frequency, SPD is applied to the sample surface, which can induce a deeper hardened layer and a larger compressive RS [21], and then improve the fatigue performance of the parts [22]. Through the USRP treatment of 40Cr steel, Wang et al. [23] discovered that the USRP can not only increase the surface microhardness of the sample by 52.6%, but also obtain a residual compressive stress of -846 MPa. In addition, the comparative wear test showed that the USRP can enhance wear resistance and lower the friction coefficient. Moreover, the surface roughness was reduced to 0.06 μm. Li et al. [24] discussed the influence of the mechanical properties of 304 stainless steel with different microstructures on the cavitation resistance after USRP and the microscopic mechanism of cavitation resistance of 304 stainless steel with different times of USRP treatments. It was discovered that the USRP, by creating a layer of grain refinement, increasing surface hardness and compressive RS, and forming a passivation coating, has a protective impact on the cavitation behavior of 304 stainless steel. However, too many times of USRP treatments can also cause defects due to the transfer of too much energy. The findings demonstrated that the times of USRP treatment for 304 stainless steel to achieve the best cavitation resistance are ten times. Xu et al. [25] investigated the effect of USRP on the surface integrity and corrosion fatigue behavior of 7B50-T7751. It was discovered that, as compared to samples not treated with USRP, the average fatigue life of the samples subjected to once, three and six times of USRP treatments was enhanced by 26.46, 22.19, and 19.59 times, respectively.

Although a lot of researches has been done to determine how USRP affects the surface integrity by experimental means, the testing process is not only time-consuming and exhausting, but also cannot achieve stress field and strain field. In recent years, numerical simulation technology has gradually become an important means for scholars to study USRP technology [21]. During their research on titanium alloys, Li et al. [26] used ABAQUS simulation software to model how pressure affect RS during USRP. The authors claimed that surface RS initially rose and subsequently fell as rolling pressure was raised. When the rolling pressure was 600 N, the surface residual stress reached the maximum. The outcome of the experiment carried out demonstrated that the variation trend of the simulation results was reliable. Liu et al. [27] used FEM to research the distribution law of some physical variables during the USRP of 7050 aluminum alloy. The authors found that the surface equivalent stress, equivalent strain, and temperature field of the strengthened samples were not uniformly distributed. The equivalent strain and stress were larger in the center region than that in the edge region. The authors also claimed that the changes of equivalent strain and stress were synchronous in the early and late stages of USRP, and the

changes of equivalent strain, equivalent stress and temperature were almost synchronous in the middle and late stages of USRP.

Although the USRP has attracted the attention of some researchers, the research on the USRP of superalloys is still very scarce. In the ultrasonic mechanical surface modification process like the USRP, many problems such as the deformation degree of the surface layer of the GH4169 superalloy, the RS and the distribution of the hardened layer are still unclear. To solve these problems, the paper carried out the USRP treatment on the samples for once (USRP-1) and four times (USRP-4) respectively. Investigations were conducted to determine the impact of USRP on the surface integrity of the GH4169 superalloy. To better understand the stress and strain field of the sample during USRP, FEM was also adopted to study the USRP. The objective of the work was to offer significant and insightful recommendations for more in-depth investigation into the ultrasonic mechanical surface modification of superalloy GH4169.

2 Experiments And Materials

2.1 Materials

The material used in the paper is GH4169 superalloy, and its microstructure and chemical composition is shown in Fig. 1 and Table 1, respectively. Grain boundaries and twin boundaries are clearly visible. The raw material is characterized by the electron backscattered diffraction (EBSD) technique (Fig. 2). The grain size and grain shape can be clearly observed from Fig. 2(a). The same color indicates the same orientation, and red, green and blue indicate that the < 001>, < 101>, < 111 > directions of the grains are parallel in the normal direction of the sample coordinate system, respectively. The original grain sizes of the samples are different, and the average grain size is about 8.32 μm (Fig. 2(c)). The grain size is mainly concentrated between 5 μm and 10 μm, but there are also some grain sizes exceeding 20 μm. Figure 2(b) presents the grain boundary misorientation distribution of GH4169 superalloy. Among them, the red solid line indicates that the corner axis is 60º/<111 > twin boundaries, and the twin boundaries account for about 40%. The high angle grain boundaries (HAGBs) are represented by the black line, and the grain boundary misorientation is greater than 15°. The low angle grain boundaries (LAGBs) are represented by the green line, and the grain boundary misorientation is between 2° and 15°. Through statistical analysis, the proportion of LAGBs is only 5.9%, and the rest are HAGBs (Fig. 2(d)).

Table 1
Chemical composition of GH4169 superalloy (wt%).

Ni	Cr	Al	Ti	C	Fe	S	Si	Nb	Mo
Balance	18.5	0.65	1.02	0.05	18.8	0.002	0.12	4.85	2.96

2.2 USRP treatment

The special equipment for USRP is presented in Fig. 3. An ultrasonic generator for producing high frequency energy, a pressing device for exerting static pressure to maintain the ball's constant contact with the surface of the workpiece, and a piezoelectric transducer for producing ultrasonic vibrations are all included in the apparatus. Among these, a relatively tiny hydraulic unit that feeds fluid into the machinery and maintains the ball's constant contact with the surface of the workpiece is responsible for creating the static pressure. After applying static pressure, the transducer transforms the electrical energy from the ultrasonic generator into ultrasonic vibrations, which are imposed on the surface of the workpiece as the balls move over it. When the rolling ball begins to move along the surface of the workpiece, the ball is free to rotate while maintaining a constant pressure. In addition, there is always an oil film on the surface of the balls and the workpiece during the strengthening process. During this USRP, the rolling ball applied a static pressure of 500 N along the normal direction of the workpiece surface, where the ultrasonic frequency in the experiment was 28 kHz and the amplitude was 12 μm. The workpiece speed is 200 r/min, and the feed rate of the rolling ball is 0.1 mm/r.

2.3 Surface morphology and microstructure characterization

The cross-sectional morphologies of the samples were observed by a high-resolution RISE-MAGNA SEM (TESCAN, CR) before and after USRP. The grain size and shape, as well as misorientation angle were analyzed using MIRA3 LHM scanning electron microscope (TESCAN, CR) coupled with fast electron backscatter diffraction. The surface roughness was characterized by using an LSM 900 laser scanning confocal microscope (Carl Zeiss AG, Germany).

2.4 Residual stress and microhardness measurement

RS detection was performed using an LXRD-type X-ray analyzer (Proto Industrial, Canada). Measurement of the displacement of the diffraction line is the fundamental idea behind RS measurement by XRD, and then use Hooke's law to calculate the residual stress [28]. The strain of the (311) plane (151.888 Bragg angle) was determined using Mn-Kα. The following specific test circumstances apply: the tube voltage is 30 kV, the tube current is 25 mA, the diameter of the collimating tube is 1 mm, the ψ angle setting range is 0º~ 45º, 8 tilt angles on one side, a total of 17 stations, and the ψ swing angle of each station is ± 3°. To measure the in-depth distribution of RS, the material of the surface layer is removed by electropolishing, and the detection is carried out according to the standards of ASTM-E915-2010, EN15305-2008 and GB7704-2017. The microhardness of the material was characterized by a nano-indenter, and the instrument used in the nanoindentation experiment was U9820A Nano Indenter G200 (Agilent Technologies, America). The highest indentation force is 0.1 N, and the holding time of the maximum load is 10s.

3 Finite Element Simulation

3.1 Finite Element Model

The FEM of USRP was established by ABAQUS simulation software. Considering that the existing simulation software cannot effectively realize the superposition of force and displacement on the rolling ball, the simulation model is divided into three steps. In the first step, a downward displacement is applied to the rolling ball, so that the contact pressure between it and the sample reaches 500 N. In the second step, ultrasonic vibration with an amplitude of 12 μm and a frequency of 28 kHz is applied to the surface of the sample on the basis of the first step. The feeding speed of the sample in the longitudinal direction is 0.33 mm/s, and the rotational speed in the circumferential direction is 20.94 rad/s. The third step is to perform spring back after USRP, so that the RS of the sample achieves a stable state. The method of face-to-face contact is selected in FEM. The sample surface serves as the secondary surface, with the rolling ball surface serving as the primary surface. To avoid penetration during contact, the typical contact behavior between the rolling ball and the sample is adjusted to hard contact. With a friction coefficient of 0.1, the rolling ball's tangential contact behavior with the sample is set to penalty contact. The rolling ball is set as a rigid body since its hardness is greater than that of the sample.

A linear reduced-integration element type (C3D8R) is used since the ultrasonic rolling simulation is a very nonlinear contact analysis procedure. Because linear reduced-integration elements have an integration point at the center of the element, there is an "hourglass" numerical problem. Therefore, the hourglass control is introduced in the linear reduced-integration element. After meshing, the entire model includes 359758 elements and 402988 nodes. The middle annular area (the axial length is 2 mm) is selected as the area of interest, and the mesh is refined in the axial and circumferential directions (Fig. 4(b)). Gradient division is performed for the mesh in the layer depth direction (radial direction) until the depth of the layer reaches 1 mm, including a total of 13 layers of nodes. In the XOY plane, the mesh size at a depth of 200 μm is about 100 μm × 50 μm, and the mesh size at a depth of 500 μm is about 100 μm × 100 μm. In the XOZ plane, the mesh size is about 100 μm × 50 μm in the middle zone and about 50 μm × 100 μm at the two sides. This meshing method can achieve a good balance between computational cost and solution accuracy. The default coordinate system in ABAQUS is the cartesian coordinate system (XYZ). However, the workpiece itself is a cylinder. To better extract the calculation results in the post-processing process, it is necessary to transform the workpiece into a cylindrical coordinate system (RTZ). The radial, circumferential, and axial stress are represented by the three stress components S11, S22, and S33, respectively.

3.2 Material model

Table 2 displays the mechanical characteristics of GH4169 superalloys and rolling balls. GH4169 superalloy adopts the Johnson-Cook (J-C) constitutive model.[29] The J-C constitutive model is the most widely used material flow stress model for plastic materials, which is a function including strain, strain rate and temperature. The function expression is as follows:

$$\sigma\left(\varepsilon_p,\dot{\varepsilon},T\right)=\left(A+B\varepsilon_p^n\right)\left[1+C\ln\left(\frac{\dot{\varepsilon}}{\dot{\varepsilon}_0}\right)\right]\left[1-\left(\frac{T-T_r}{T-T_m}\right)^m\right]$$

1

where *A*, *B*, *n*, *C* and m represent the initial yield stress, hardening modulus, strain hardening exponent, strain rate strengthening parameter and thermal softening exponent, respectively; ϵ_p $\dot{\epsilon}_0$ T_r and T_m represent the equivalent plastic strain, the reference strain rate, the reference temperature (usually room temperature) and the melting temperature, respectively.

Table 2
Material physical properties.

Materials	Density (g/cm^3)	Elastic Modulus (MPa)	Poisson's Ratio	Thermal Conductivity W/(m·K)	Specific Heat (mJ/ton·K)
Carbide [30]	1.5	800000	0.2	46	2.03e^8
GH4169 [31]	8.2	210000	0.3	11.4	4.35e^8

To obtain the JC constitutive parameters, dynamic compression tests are carried out in the system of Hopkinson compression bars, and tests for strain rates is 3000 s^{-1}, 5000 s^{-1}, 8000 s^{-1}, 10000 s^{-1}, and tests for temperatures is 30°C, 300°C, 500°C, 800°C.

(1) Solve the parameter *A*, *B* and *n*

First, the flow stress data of the quasi-static mechanical test is obtained, and the Eq. (1) is converted into the Eq. (2), and next calculating the logarithm of both sides of the Eq. (2) can obtain the fitting Eq. (3). *A* is the yield stress of the material. At this time, is a linear function of ln(σ-A), and the parameter values of *B* and *n* can be obtained by linearly fitting the quasi-static tensile experimental data.

$$\sigma = A + B \cdot \varepsilon_p^n$$

2

$$\ln(\sigma - A) = \ln B + n \cdot \ln \varepsilon_p$$

3

(2) Solve the parameter *C*

When the Hopkinson pressure bar test is carried out at room temperature, $T = T_0$, Eq. (1) is converted into Eq. (4).

$$\frac{\sigma}{A + B \cdot \varepsilon^n} = 1 + C \cdot \ln \frac{\dot{\varepsilon}}{\dot{\varepsilon}_0}$$

4

Substitute the SHPB flow stress and strain data at four strain rates of 3000 s^{-1}, 5000 s^{-1}, 8000 s^{-1} and 10000 s^{-1} at room temperature, and perform linear fitting on the flow stress data when the strain ε is a certain value, and finally value of *C* can be obtained.

(3) Solve the parameter *m*

Finally, logarithmically transform Eq. (1) into a linear equation of *m*, such as Eq. (5).

$$\ln\left(1-\frac{\sigma}{[A+B\cdot\varepsilon^{\mathrm{n}}]\cdot[1+C\cdot\ln\dot{\varepsilon}^{*}]}\right)=\mathrm{m}\cdot\ln\frac{T-T_r}{T-T_m}$$

5

Through the above regression analysis process, the J-C constitutive model parameters can be obtained, as shown in Table 3.

Table 3
J-C strength model constants for GH4169

A(MPa)	B(Mpa)	C	n	m
1170	1416	0.003	0.69	1.05

4. Results And Discussion

4.1 Surface morphology and surface roughness

Figure 5 shows the SEM images of the BM and USRP treated samples. the surface of the BM has obvious feed marks caused by turning process, which can cause stress concentration (Fig. 5(a)). After USRP treatment, the feed marks on the surface have been completely removed (Fig. 5(b)). However, impact-induced creases and hollows appear on the surface of the sample.

The surface three-dimensional topography of the samples before and after USRP are measured by the Zeiss scanning laser confocal microscope. Figure 6 shows the machined surface topography of the BM and USRP treated samples. The machined surface appears obvious cutting marks, showing a wavy shape (Fig. 6(a)). After USRP treatment, the surface of the sample has no cutting marks, and the features of peaks and valleys after turning are also eliminated, indicating that USRP treatments achieve the effect of "cutting peaks and filling valleys" (Fig. 6(b-c)). The surface roughness decreases obviously after USRP treatment. After USRP-1 treatment, Ra decreases from about 1.17 um to 0.08 um, a decrease of 93%, indicating a considerable reduction in surface roughness. Different from uneven surface topography caused by SP [36], USRP treatment achieves better surface integrity, which increases the fatigue property of materials.

4.2 Surface layer Microstructure

Electron Backscattered Diffraction (EBSD) is an advanced characterization technique that is particularly useful for researching processing-induced deformation, providing theoretical information on grain size as well as grain boundary misorientation.[32] The quality of the Kikuchi diffraction pattern is degraded by the presence of deformations and refined structures, resulting in a higher number of unindexed pixels in the surface layer. Figure 7(a) and (b) show EBSD images of USRP-1 and USRP-4-treated surface layer, respectively. The grains of the surface layer are obviously refined and deformed after USRP treatment. Especially for the USRP-4 treated samples, the grain refinement and deformation layer are very obvious, which indicates that USRP treatment can decompose the coarse grains into fine grains. Due to the effect of ultrasonic shock, the grains are gradually elongated and rotated along the sliding shear direction, and the grain boundaries are also severely bent and elongated. With an increase in USRP treatment time, grain deformation becomes more severe. Moreover, the degree of grain deformation lessens as one moves away from the surface until one reaches an undeformed area. Following the statistical evaluation of grain size, as the time of USRP treatment increases from once to four times, the grain size of the surface layer decreases from 6.74 μm to 4.78 μm, a decrease of 29.1%. (Fig. 7(c) and (d)).

Figure 8(a) and (b) present the grain boundary misorientation distribution maps of USRP-1 and USRP-4, respectively. Figure 8 shows that the USRP treatment produces a high density of LAGBs in the surface layer, and the proportion of twin boundaries with a rotation angle axis of 60º/<111 > is significantly reduced. During the USRP treatment, a large number of twins were broken and recrystallized grains were formed. When the time of USRP treatments increases from once to four times, the proportion of twins with a rotation angle axis of 60º/<111 > decreases from 6.2–4.3%. The density and depth of the LAGBs also increase significantly with the increase in the time of USRP treatments. After USRP-1 treatment, the number proportion of LAGBs in the surface layer reaches 70.8%. After USRP-4 treatments, the number proportion of LAGBs in the surface layer reaches 85.5%.

To understand the dislocation strengthening effect, the distribution maps of Kernel Average Misorientation (KAM) and Geometrically Necessary Dislocation (GND) after different USRP treatments are showed. KAM stands for local misorientation and indicates how homogenized the plastic deformation is. When the KAM value is small, it means that the degree of plastic deformation and defect density are small. From Fig. 9 (a) and (b), the average KAM value increases from 0.98º for the USRP-1 treatment to 1.55º for the USRP-4 treatment with the increase of the time of USRP.

The GND can be calculated by Eq. (6):

$$\rho^{GND} = \frac{KAM}{\mu b}$$

6

Where b is the Buiger vector and μ is the scan step size of the EBSD image. According to the GND calculation formula, it can be known that the change rule of GND is the same as the that of KAM. The time of USRP treatment has a significant impact on GND. In addition, the regions of high dislocation density all occur at grain boundaries. Sakai et al. [33] demonstrated that the formation of LAGBs is associated with the accumulation of GND. Yu et al.[34] showed that the true dislocation density and GND have the same trend of change. Therefore, the true dislocation density increases with the increase of the time of USRP treatments.

3.3 Microhardness

To interpret the strengthening effect of USRP treatment on the samples, the hardness was characterized by means of nanoindentation. Figure 11 illustrates that when the distance from the machined surface rises, the microhardness steadily decreases after turning process. The depth of the hardening layer induced by turning process is about 50 μm, and the maximum microhardness is about 6.2 GPa. USRP treatment produces a hardened layer depth of 0.6 mm. The microhardness increases from about 5.98 GPa of the matrix material to about 6.7 GPa of the surface, an increase of 12%. The microhardness initially rises and subsequently falls to the hardness of the matrix material as the distance from the free surface increases. The maximum microhardness appears at the subsurface layer, and the value is about 6.8 GPa. Some scholars [40] believe that the microhardness of the machined surface area is lower than that of the subsurface area on account of the edge effect. In addition, the microhardness increases slightly with the increase of the time of USRP treatment, meaning that the degree of work hardening also increased with the increase of the number of USRP treatment.

4.4 Residual stress

Figure 12 presents the results of RS measured by XRD. The axial and circumferential compressive RS of the BM sample decreases with the increase of the distance from the surface (Fig. 12(a) and (b)). The axial compressive RS of the sample after USRP treatment decreases with the distance from the surface increases. However, when the depth from the surface increases, the circumferential compressive RS initially rises and then falls. The depth of the axial and circumferential compressive RS of the BM sample is about 50 μm, while the depth of the axial and circumferential compressive RS of USRP treated samples reaches about 600 μm. USRP treatment can increase the surface axial compressive RS from − 327.5 MPa to -1012 MPa ~ -1093.5 MPa, an increase of 209% ~ 234%. RS is not significantly impacted by the time of USRP treatments.

Full width at half maximum (FWHM) is regarded as a measure of the micro-strain brought on by mechanical processing. It has long been common practice to describe work hardening following surface treatment techniques using the FWHM of XRD peaks. The level of plastic deformation can be estimated from the change in FWHM [35, 36]. Figure 13 summarizes the variation rule of the XRD peak FWHM of the samples along the depth direction. By comparing the peak widths before and after USRP treatment, it can be found that the change rule of the FWHM is similar to the influence depth of the compressive RS along

the axial direction in Fig. 13, and it rapidly declines with the increase of the depth. For the BM samples, the plastic working zone extends to around 50 μm. For the USRP treated samples, the plastic deformation zone extends to around 600 μm (Fig. 13(a) and (b)).

4.5 Finite element simulation results

The stress contour plot of the longitudinal section (XOY) of the sample obtained by FEM are shown in Fig. 14. The S22 stress contour plots show that the circumferential RS from the surface to the center of the circle changes from compressive stress to tensile stress, and the magnitude of the compressive RS near the surface is larger than the that of the internal tensile RS. The axial RS distribution from the surface to the center of the circle is similar to the circumferential RS, changing from compressive stress to tensile stress. When the time of USRP treatments reaches four times, the stress distribution trend does not change significantly. According to Fig. 15, the magnitude of residual stress of the USRP-4 treated sample is larger than that of the USRP-1 treated sample, but the stress-affected zone is almost unchanged.

In addition, the plastic strain contour plot of the longitudinal section (XOY) is selected for analysis (Fig. 16). The maximum equivalent plastic strain of USRP-1 treated samples is 0.18, while the maximum equivalent plastic strain of USRP-1 treated samples is 0.25. The degree of plastic deformation gradually decreases with the increase of the depth from the surface. Figure 17 shows that the depth of the plastic strain layer of USRP-4 treated samples is consistent with that of the USRP-1 treated samples, reaching about 0.6 mm. However, the magnitude of equivalent plastic strain of the USRP-4 treated sample is larger than that of the USRP-1 treated sample.

5 Conclusion

The following findings are made from this study on the impact of USRP on the surface integrity of GH4169 superalloy, which used experimental and finite element approaches.

(1) The USRP process can completely remove the feed marks generated by the previous turning process. The surface roughness of the samples decreases from 1.17 μm to 0.08 μm, a decrease of more than an order of magnitude.

(2) The USRP treatment can significantly refine the grains of the machined surface layer, and the grain size reduces from 8.32 μm in the matrix material to 4.78 μm. USRP treatment can also form a large number of LAGBs in the machined surface layer. The density of LAGBs increases with the time of USRP treatments. Furthermore, the dislocation density also increases with the time of USRP treatments.

(3) USRP treatments result in a work hardened layer and compressive RS layer with a depth of 1 mm and 0.6 mm, respectively. The maximum compressive RS of the surface reaches − 1102 MPa, and the maximum microhardness of the surface is 6.97 GPa. The axial compressive RS decreases while the

circumferential compressive RS initially rises and subsequently falls with the increase of the depth from the surface.

(4) The RS obtained by the established FEM are consistent with the experimental results, indicating the accuracy and reliability of the FEM.

Declarations

Funding: The investigation was supported by National Science and Technology Major Project (Y2019-VII-0018-0160).

Availability of data and material: The raw/processed data required to reproduce these findings cannot be shared at this time as the data also forms part of an ongoing study.

Code availability: not applicable.

Authors' contributions: Weiwei Yu, Qinglong An, Ming Chen, Haowei Wang and Dong Chen had designed the framework and research route of the whole work; Weiwei Yu and Jie Wu had conducted the experimental operations; Weiwei Yu had accomplished the data treatment and analysis; Weiwei Yu and Ming Chen had finished the organization and writing work of the paper; all authors discussed the results and they had revised and modified the manuscript.

Acknowledgments: We thank State Key Laboratory of Metal Matrix Composites for providing USRP treatment, and we thank other members of the laboratory who made suggestions during the experimental process and the paper formation process.

Compliance with ethical standards

Conflicts of interest/Competing interests: The authors declare that they have no conflict of interest.

Ethical approval: This paper is new. Neither the entire paper nor any part of its content has been published or has been accepted elsewhere. It is not being submitted to any other journal as well.

Consent to participate: Not applicable.

Consent to publish: Not applicable.

References

1. Roy S, Kumar R, Anurag, Panda A, Das RK (2018) A Brief Review on Machining of Inconel 718. Materials Today: Proceedings 5 (9, Part 3):18664–18673
2. Liu YM, Wang L, Chen G, Li BB, Wang XH (2019) Investigation on ratcheting-fatigue behavior and damage mechanism of GH4169 at 650 ℃. MAT SCI ENG A-STRUCT 743:314–321

3. Zhang X-C, Li H-C, Zeng X, Tu S-T, Zhang C-C, Wang Q-Q (2017) Fatigue behavior and bilinear Coffin-Manson plots of Ni-based GH4169 alloy with different volume fractions of δ phase. MAT SCI ENG A-STRUCT 682:12–22
4. Kumar KS, Van Swygenhoven H, Suresh S (2003) Mechanical behavior of nanocrystalline metals and alloys11The Golden Jubilee Issue—Selected topics in Materials Science and Engineering: Past, Present and Future, edited by S. Suresh. ACTA MATER 51 (19):5743–5774
5. Chai G, Forsman T, Gustavsson F (2016) Microscopic and nanoscopic study on subsurface damage and fatigue crack initiation during very high cycle fatigue. INT J FATIGUE 83:288–292
6. Liu YG, Li MQ, Liu HJ (2017) Nanostructure and surface roughness in the processed surface layer of Ti-6Al-4V via shot peening. MATER CHARACT 123:83–90
7. Martinez SA, Sathish S, Blodgett MP, Mall S, Namjoshi S (2005) Effects of fretting fatigue on the residual stress of shot peened Ti-6Al-4V samples. MAT SCI ENG A-STRUC 399(1–2):58–63
8. Zhou J, Sun Z, Kanoute P, Retraint D (2017) Effect of surface mechanical attrition treatment on low cycle fatigue properties of an austenitic stainless steel. INT J FATIGUE 103:309–317
9. Li Q, Yan FK, Tao NR, Ponge D, Raabe D, Lu K (2019) Deformation compatibility between nanotwinned and recrystallized grains enhances resistance to interface cracking in cyclic loaded stainless steel. ACTA MATER 165:87–98
10. Lei YB, Wang ZB, Xu JL, Lu K (2019) Simultaneous enhancement of stress- and strain-controlled fatigue properties in 316L stainless steel with gradient nanostructure. ACTA MATER 168:133–142
11. Huang HW, Wang ZB, Lu J, Lu K (2015) Fatigue behaviors of AISI 316L stainless steel with a gradient nanostructured surface layer. ACTA MATER 87:150–160
12. Majzoobi GH, Azadikhah K, Nemati J (2009) The effects of deep rolling and shot peening on fretting fatigue resistance of Aluminum-7075-T6. MAT SCI ENG A-STRUC. 516:235–2471–2
13. Abrao AM, Denkena B, Kohler J, Breidenstein B, Morke T (2014) The influence of deep rolling on the surface integrity of AISI 1060 high carbon steel. In: 2nd CIRP Conference on Surface Integrity (CSI), Nottingham, ENGLAND, May 28–30 2014. Procedia CIRP. pp 31–36. doi:10.1016/j.procir.2014.04.006
14. Kattoura M, Mannava SR, Qian D, Vasudevan VK (2017) Effect of laser shock peening on elevated temperature residual stress, microstructure and fatigue behavior of ATI 718Plus alloy. INT J FATIGUE 104:366–378
15. Ye C, Suslov S, Lin D, Liao YL, Fei XL, Cheng GJ (2011) Microstructure and mechanical properties of copper subjected to cryogenic laser shock peening. J APPL PHYS 110 (8)
16. Messé OMDM, Stekovic S, Hardy MC, Rae CMF (2014) Characterization of Plastic Deformation Induced by Shot-Peening in a Ni-Base Superalloy. JOM 66(12):2502–2515
17. Nagarajan B, Kumar D, Fan Z, Castagne S (2018) Effect of deep cold rolling on mechanical properties and microstructure of nickel-based superalloys. MAT SCI ENG A-STRUCT 728:196–207

18. Kumar S, Sudhakar Rao G, Chattopadhyay K, Mahobia GS, Santhi Srinivas NC, Singh V (2014) Effect of surface nanostructure on tensile behavior of superalloy IN718. Materials & Design (1980–2015) 62:76–82
19. Hua Y, Liu Z, Wang B, Hou X (2019) Surface modification through combination of finish turning with low plasticity burnishing and its effect on fatigue performance for Inconel 718. SURF COAT TECH 375:508–517
20. Zhang Y, Huang C, Liu F, Liu F, Song M, Ke L (2021) Nanocrystallization of a Ti40 cladding layer by ultrasonic impact to improve burn resistance. J MATER RES TECHNOL 11:1331–1342
21. Li YG, Lian GH, Geng JW, Song CF, Chen D, Wang HW (2021) Effects of ultrasonic rolling on the surface integrity of in-situ TiB2/2024Al composite. J MATER PROCESS TECH 293.
22. Bozdana AT, Gindy NNZ, Li H (2005) Deep cold rolling with ultrasonic vibrations - a new mechanical surface enhancement technique. INT J MACH TOOL MANU 45(6):713–718
23. Ting W, Dongpo W, Gang L, Baoming G, Ningxia S (2008) Investigations on the nanocrystallization of 40Cr using ultrasonic surface rolling processing. Appl Surf Sci 255(5):1824–1829
24. Li CY, Zhu RT, Zhang XX, Huang PF, Wang X, Wang X (2020) Impact of surface ultrasonic rolling on cavitation erosion behavior of 304 stainless steel.Surface & Coatings Technology383
25. Xu XC, Liu DX, Zhang XH, Liu CS, Liu D, Zhang WC (2019) Influence of ultrasonic rolling on surface integrity and corrosion fatigue behavior of 7B50-T7751 aluminum alloy. INT J FATIGUE 125:237–248
26. Li FQ, Zhao B, Lan SL, Feng ZB (2020) Experiment and simulation of the effect of ultrasonic rolling on the surface properties of Ti-6Al-4V. INT J ADV MANUF TECH 106(5–6):1893–1900
27. Liu HW, Zheng JX, Guo YL, Zhu LX (2020) Residual stresses in high-speed two-dimensional ultrasonic rolling 7050 aluminum alloy with thermal-mechanical coupling.INT J MECH SCI186
28. Cullity BD (1956) Elements of X-ray Diffraction. Addison-Wesley Publishing
29. Johnson GRJPtISB (1983) A constitutive model and data for materials subjected to large strains, high strain rates, and high temperatures.541–547
30. Ozel T, Zeren E (2007) Finite element modeling the influence of edge roundness on the stress and temperature fields induced by high-speed machining. INT J ADV MANUF TECH 35(3–4):255–267
31. Pereira JM, Lerch BA (2001) Effects of heat treatment on the ballistic impact properties of Inconel 718 for jet engine fan containment applications. INT J IMPACT ENG 25(8):715–733
32. Zhou JM, Bushlya V, Peng RL, Johansson S, Avdovic P, Stahl JE (2011) Effects of Tool Wear on Subsurface Deformation of Nickel-based Superalloy. Procedia Eng 19:407–413
33. Sakai T, Belyakov A, Kaibyshev R, Miura H, Jonas JJ (2014) Dynamic and post-dynamic recrystallization under hot, cold and severe plastic deformation conditions. Prog Mater Sci 60:130–207
34. Yu H, Jin Y, Hu L, Wang Y (2020) Mechanical properties of the solution treated and quenched Al–Cu–Li alloy (AA2195) sheet during high strain rate deformation at room temperature. MAT SCI ENG A-

STRUCT 793:139880

35. Prevey PS (2000) The effect of cold work on the thermal stability of residual compression in surface enhanced IN718. In: 20th Annual Conference on Heat Treating, St Louis, Mo, Oct 09–12 2000. pp 426–434
36. Li W, Withers PJ, Axinte D, Preuss M, Andrews P (2009) Residual stresses in face finish turning of high strength nickel-based superalloy. J MATER PROCESS TECH 209(10):4896–4902

Figures

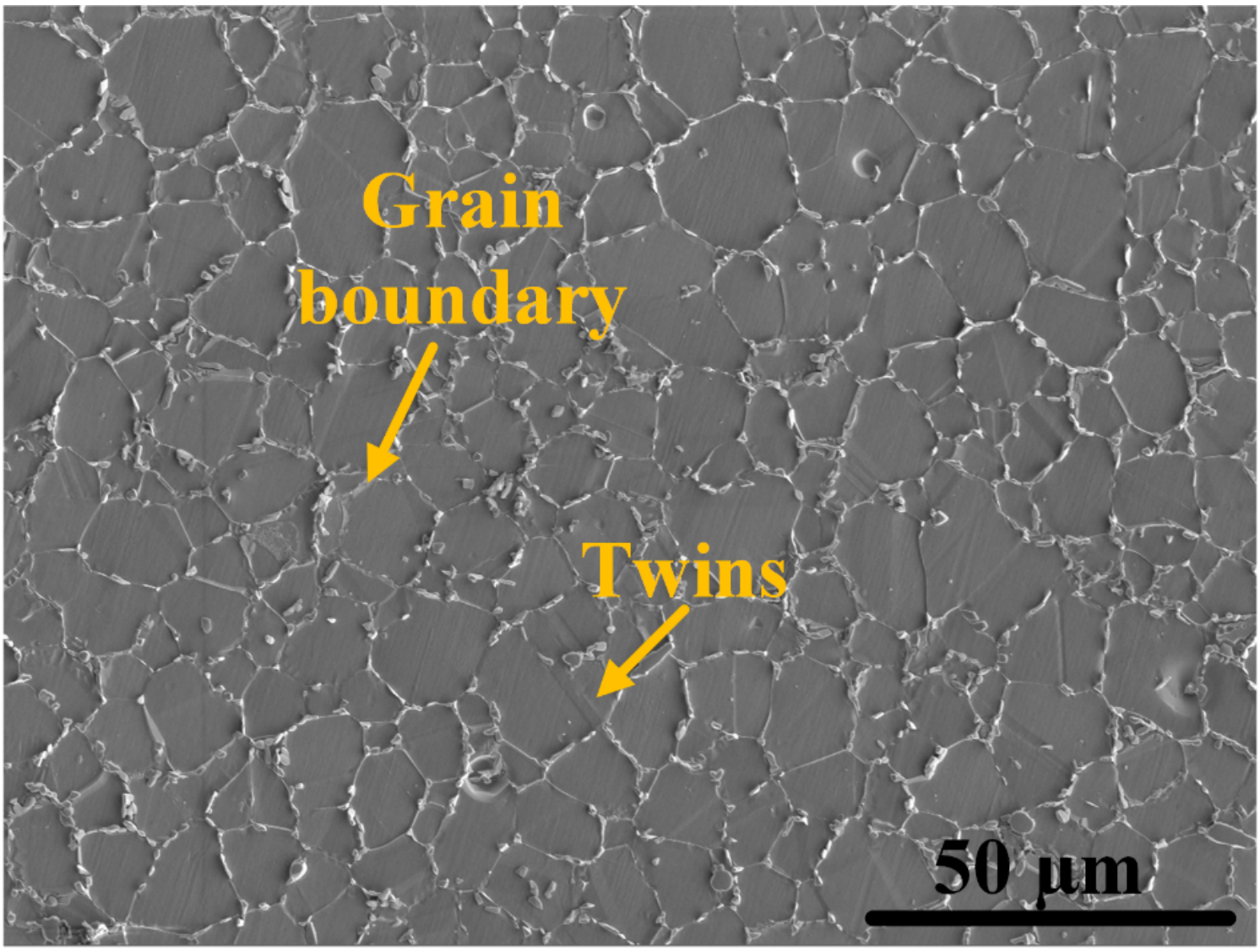

Figure 1

Microstructure of the GH4169 superalloy.

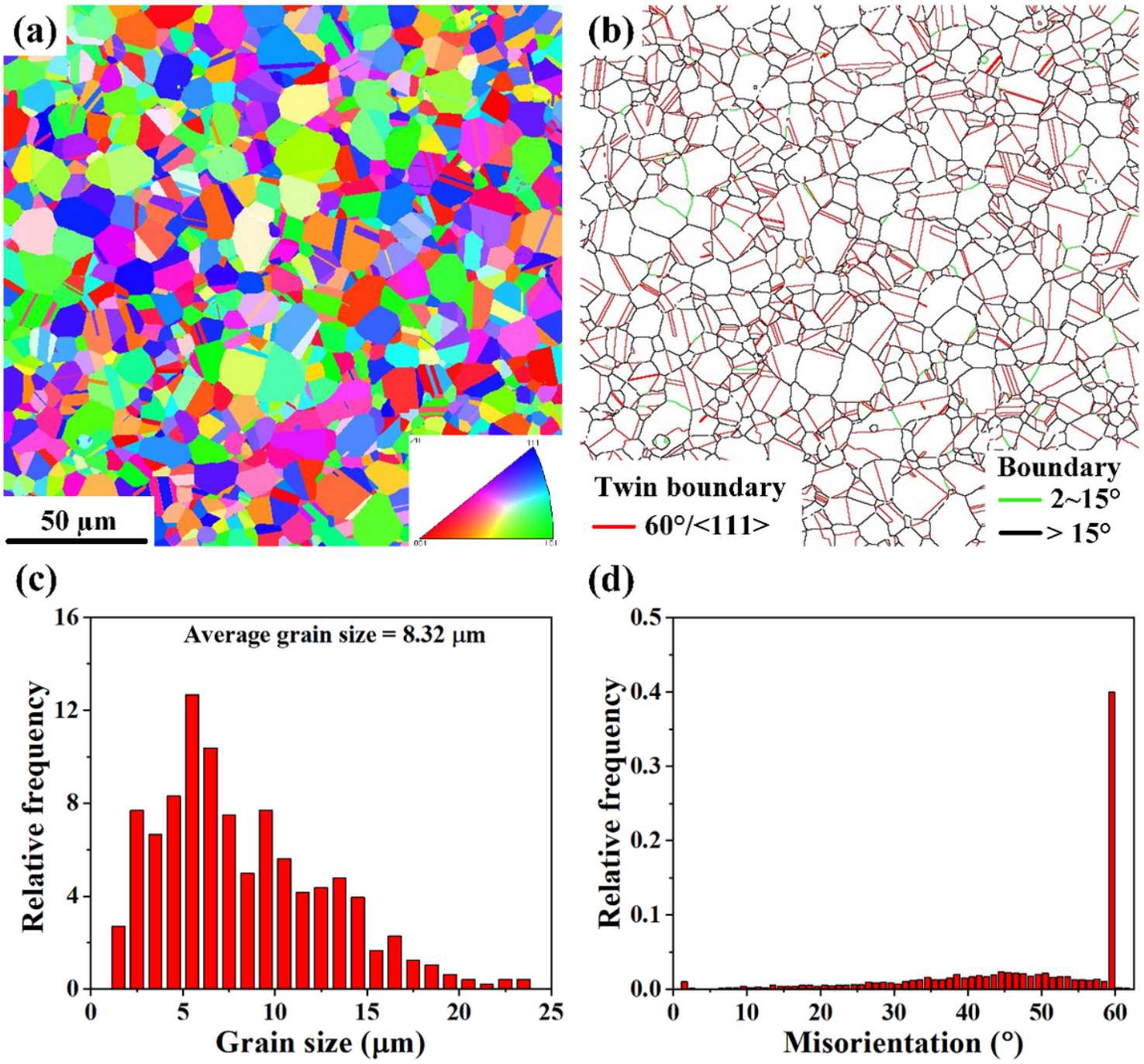

Figure 2

EBSD images of GH4169 superalloy (a) Inverse pole figure, (b) grain boundary figure, (c) distribution of grain size, (b) distribution of grain boundary misorientation.

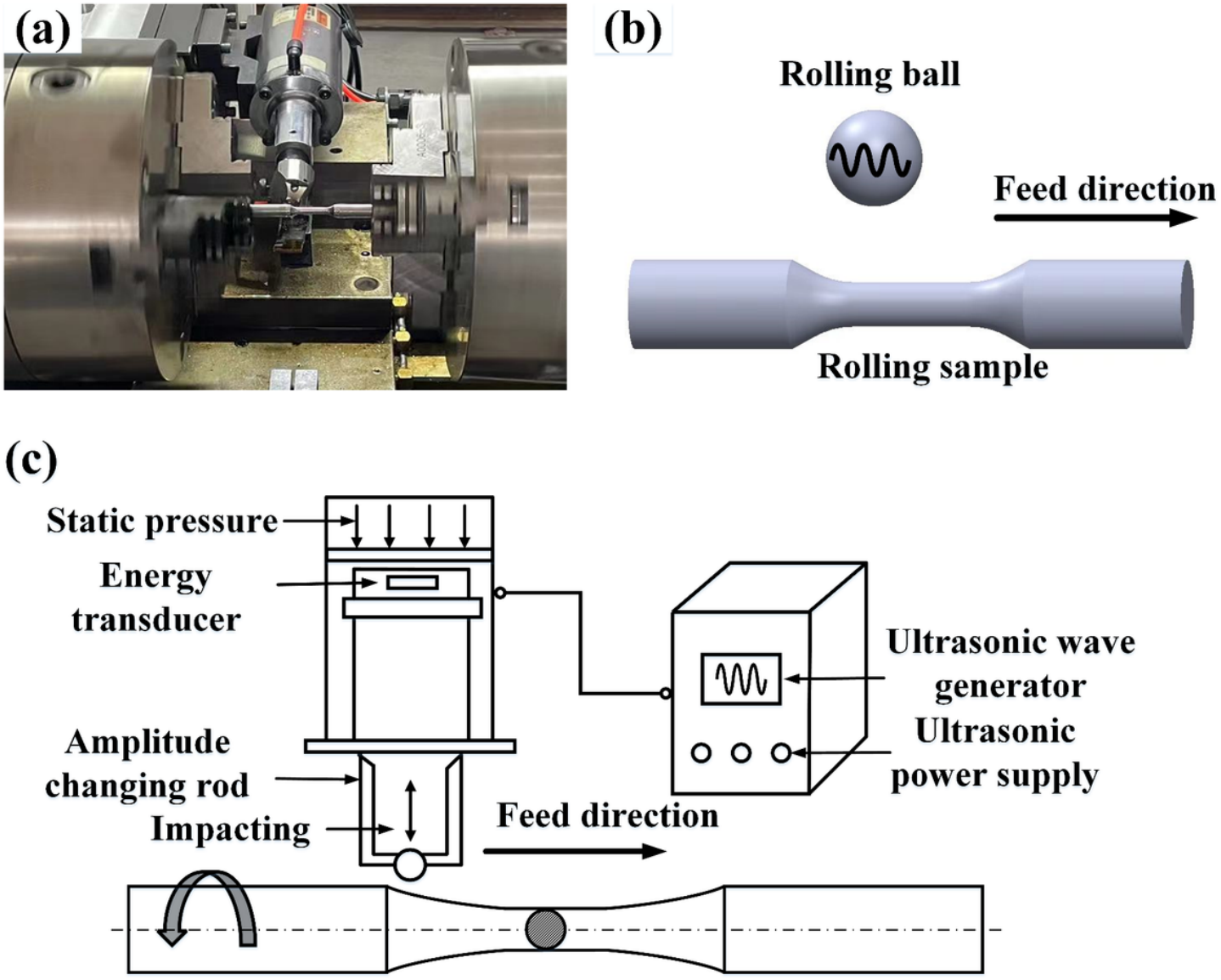

Figure 3

Experimental setup:(a) Equipment diagram of USRP; (b) Experimental detail diagram; (c) Schematic diagram of USRP.

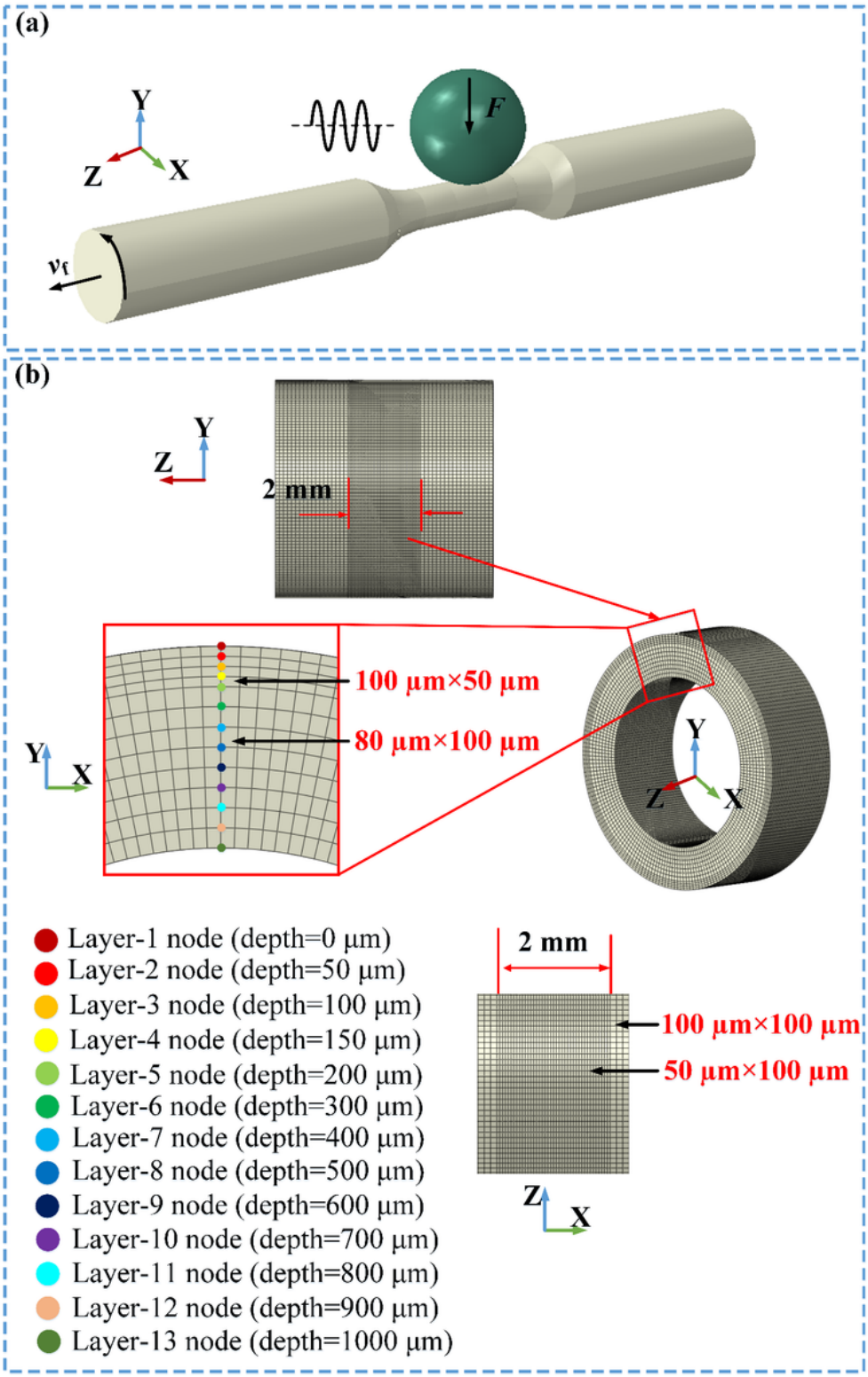

Figure 4

3D finite element model: (a) assembly schematic diagram; (b) mesh model and node assignment of interest.

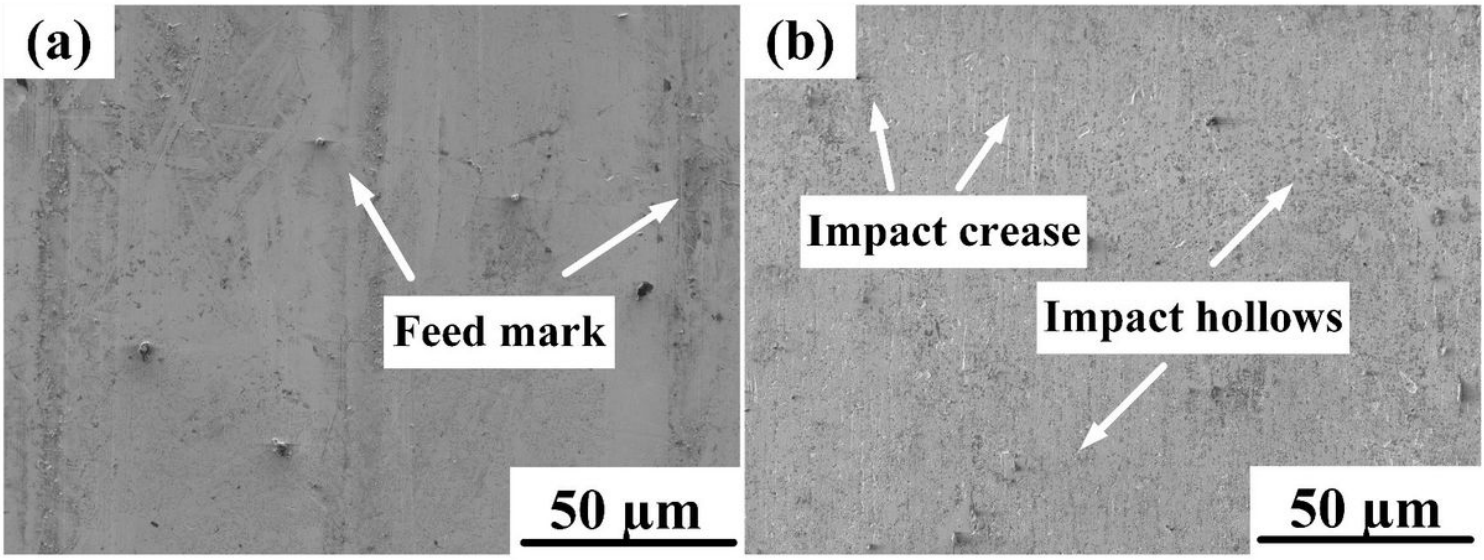

Figure 5

Surface morphologies of samples observed under SEM: (a) BM; (b) USRP treatment.

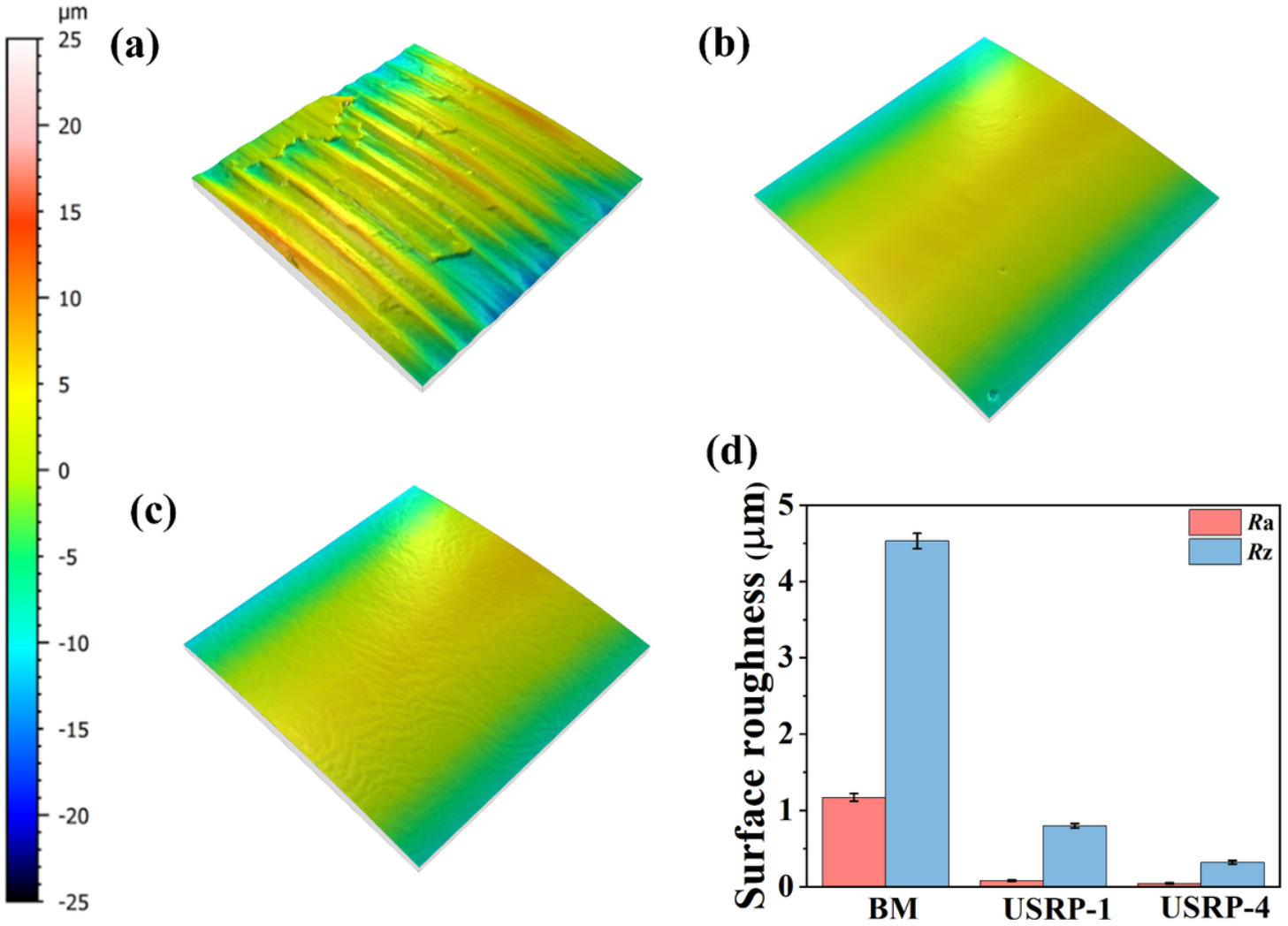

Figure 6

Surface topography and roughness: (a) BM, (b) USRP-1, (c) USRP-4

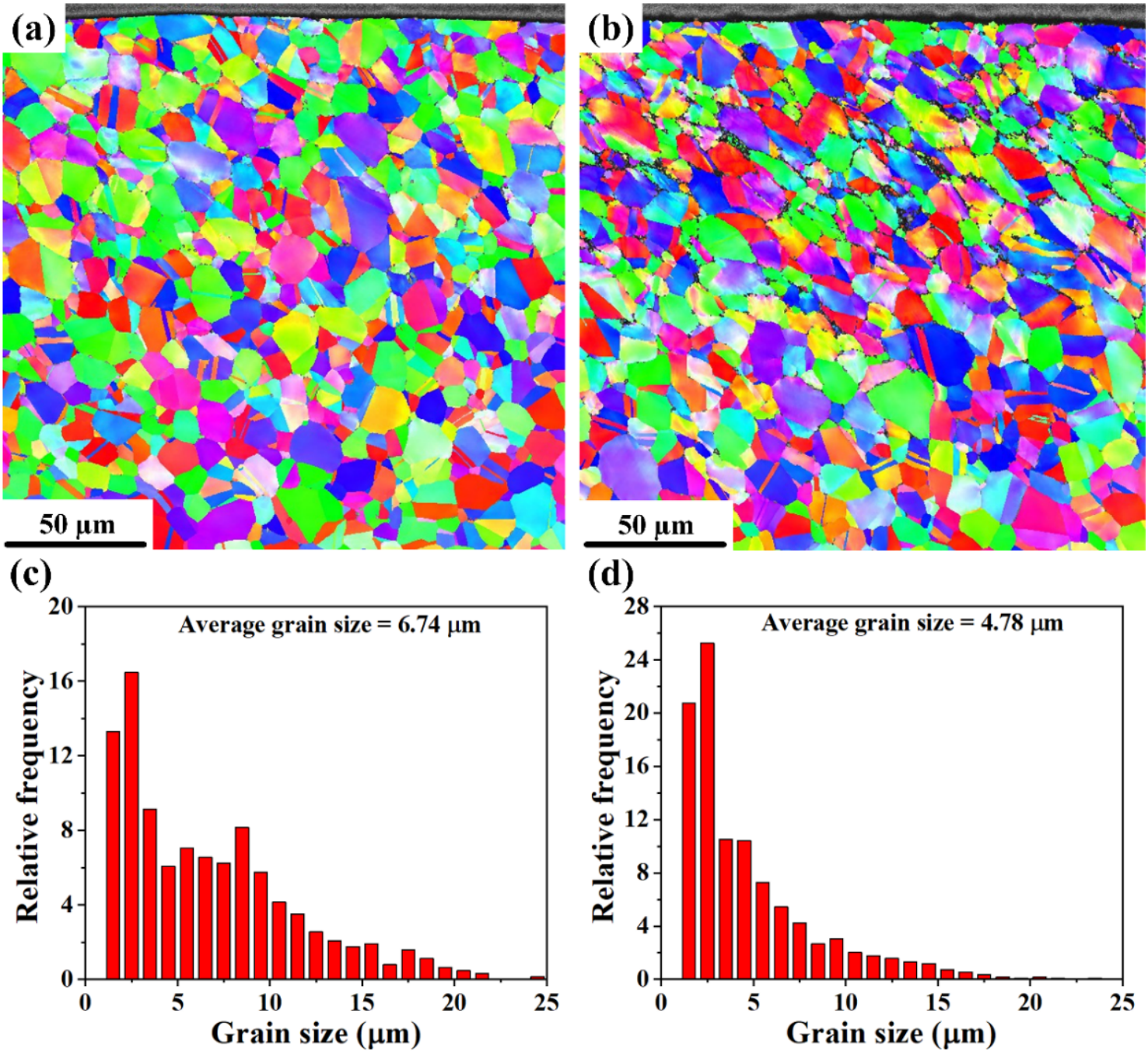

Figure 7

IPF and grain size distribution of microstructure of GH4169 superalloy treated with USRP: (a, c) USRP-1; (b, d) USRP-4.

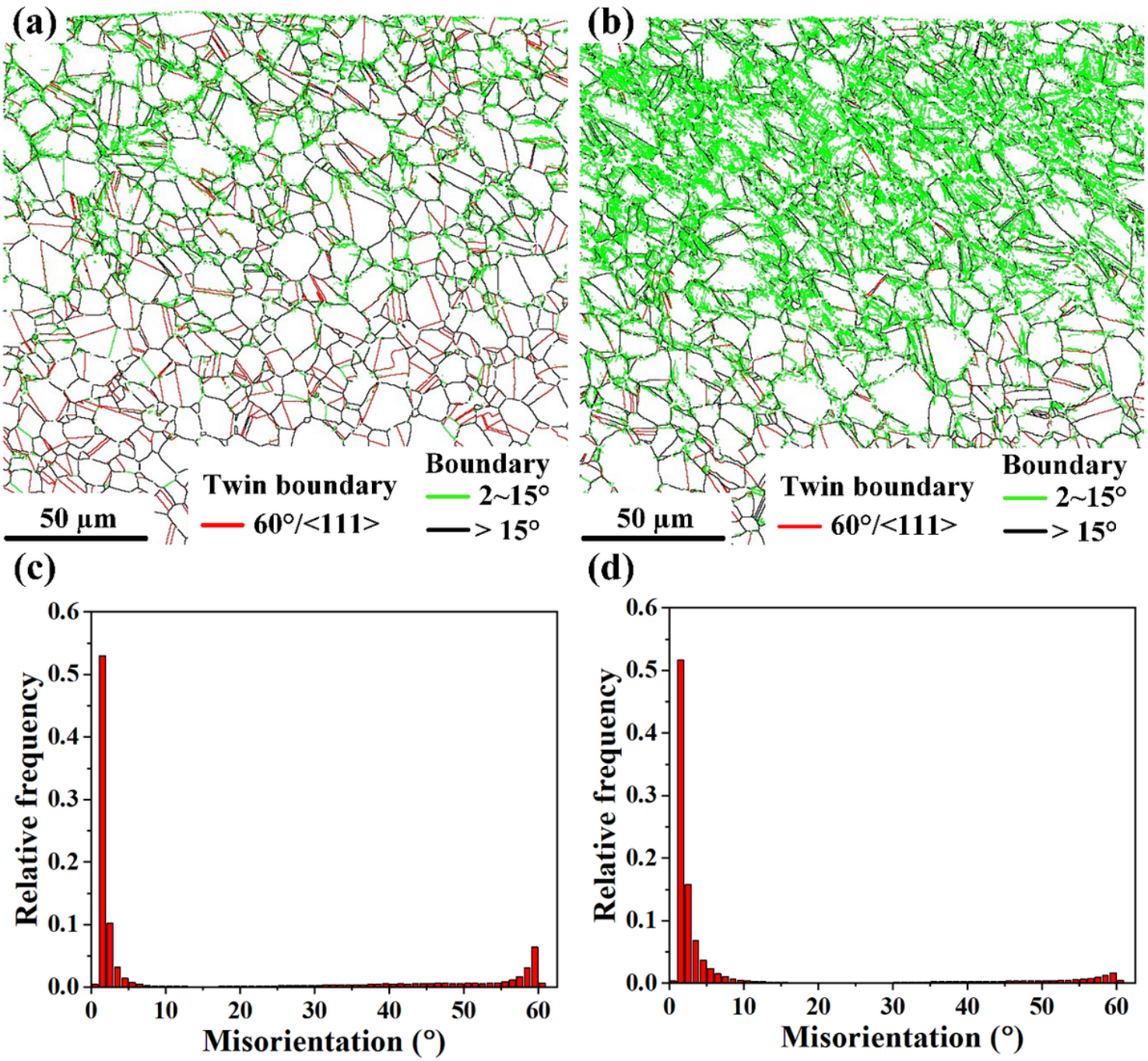

Figure 8

Grain boundary misorientation distribution of microstructure of GH4169 superalloy treated with USRP: (a, c) USRP-1; (b, d) USRP-4.

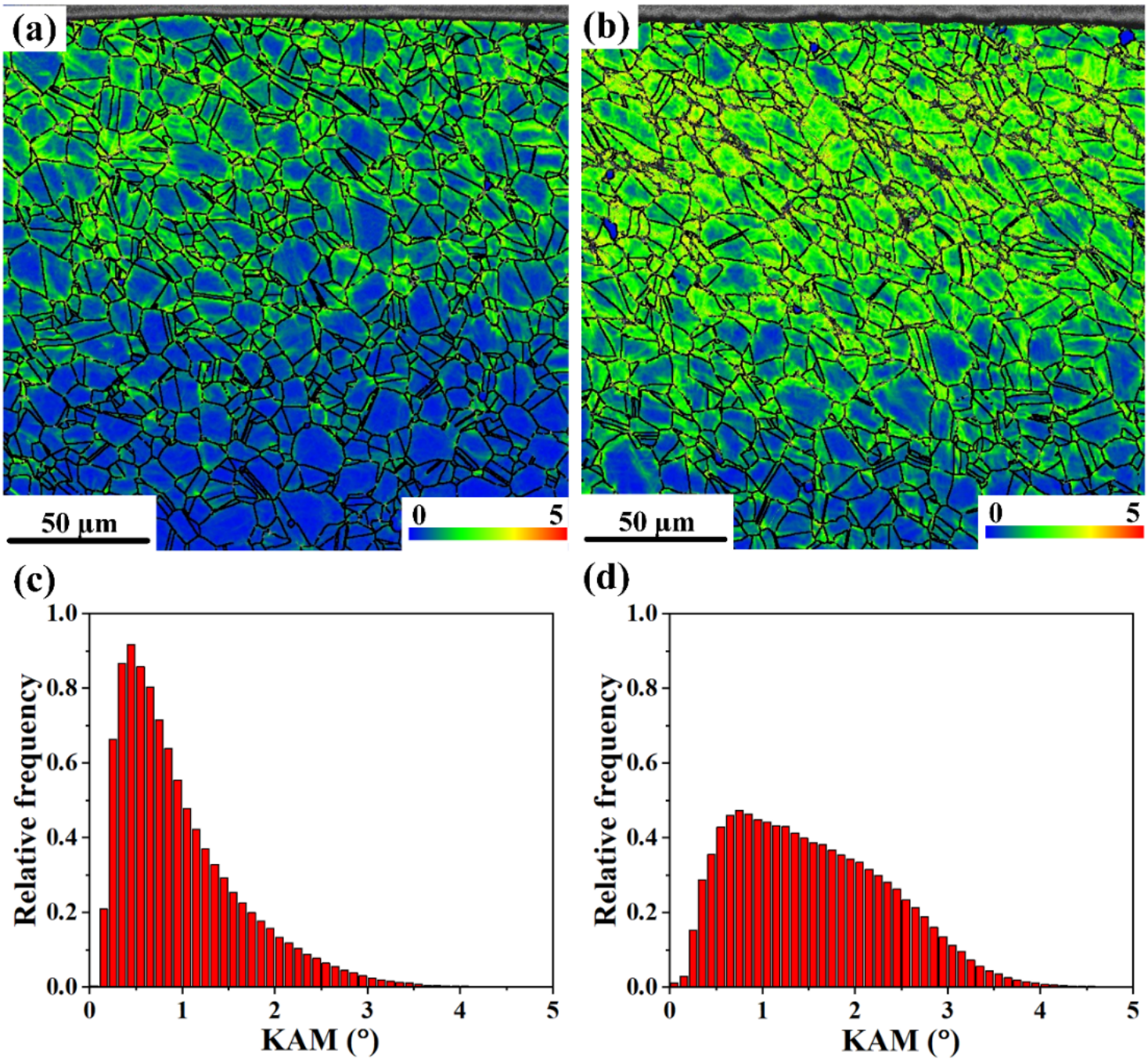

Figure 9

KAM distribution of GH4169 superalloy treated with USRP: (a, c) USRP-1; (b, d) USRP-4.

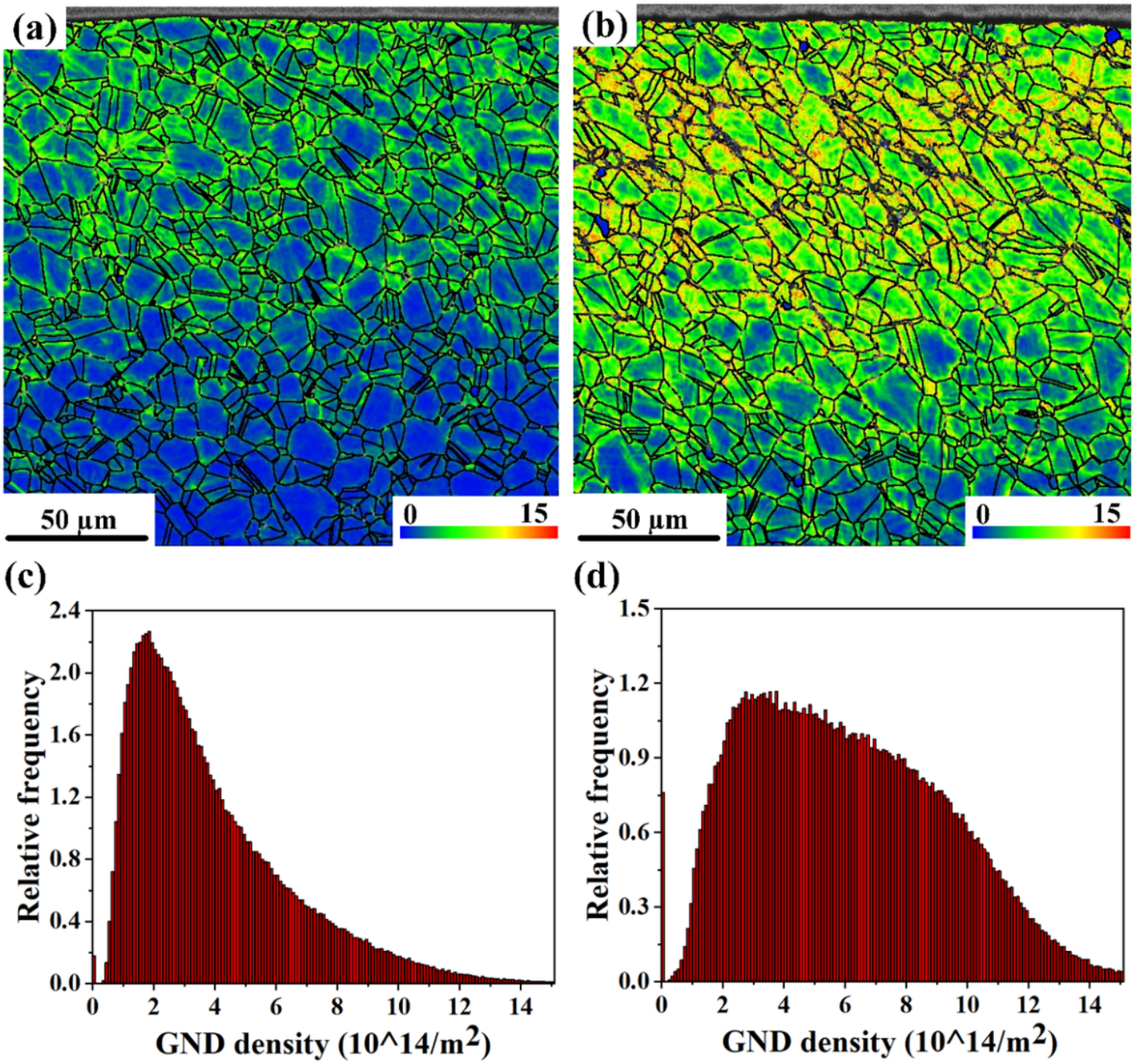

Figure 10

GND distribution of GH4169 superalloy under USRP treatment: (a, c) USRP-1; (b, d) USRP-4.

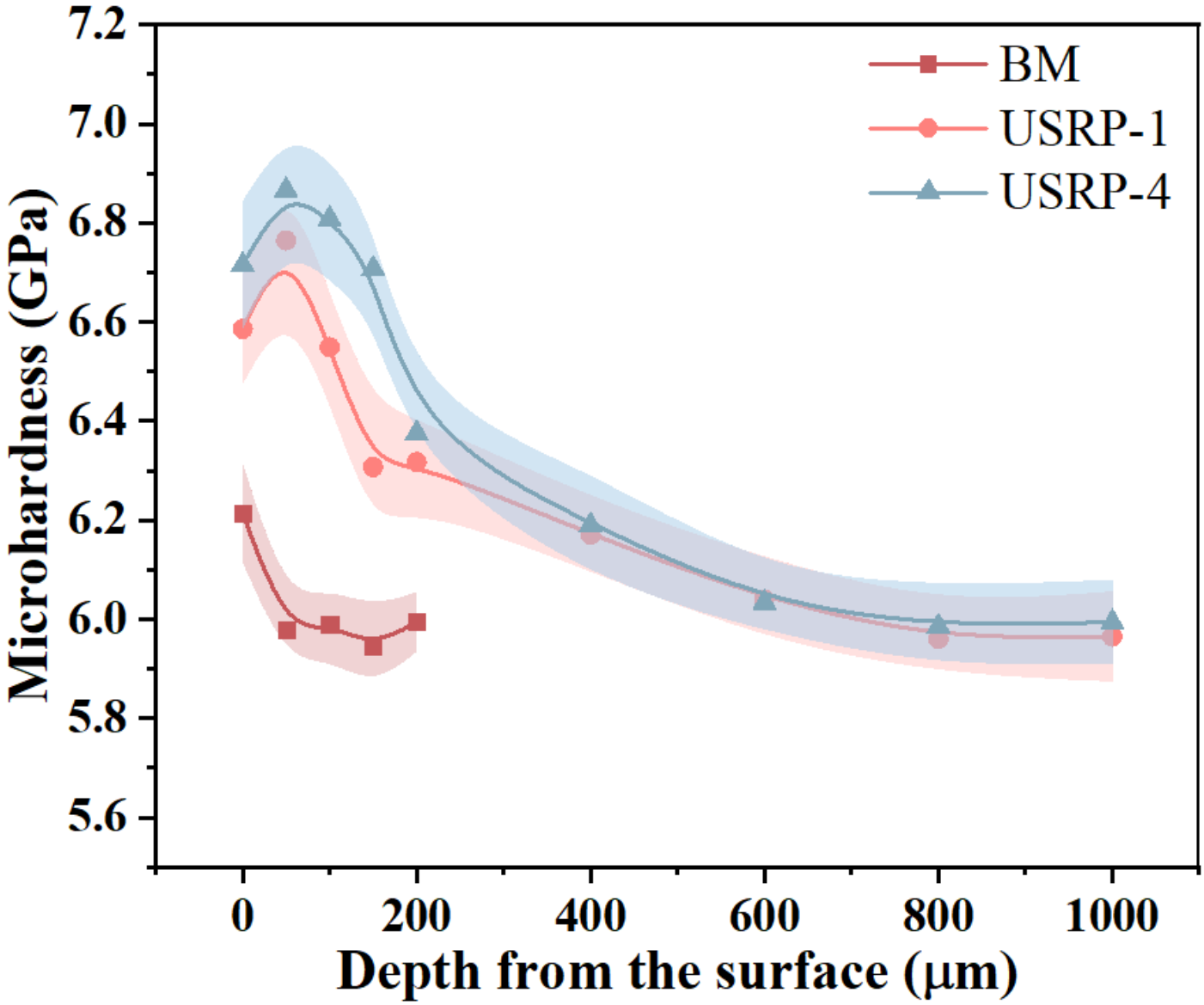

Figure 11

Microhardness Distribution along with the depth from the surface.

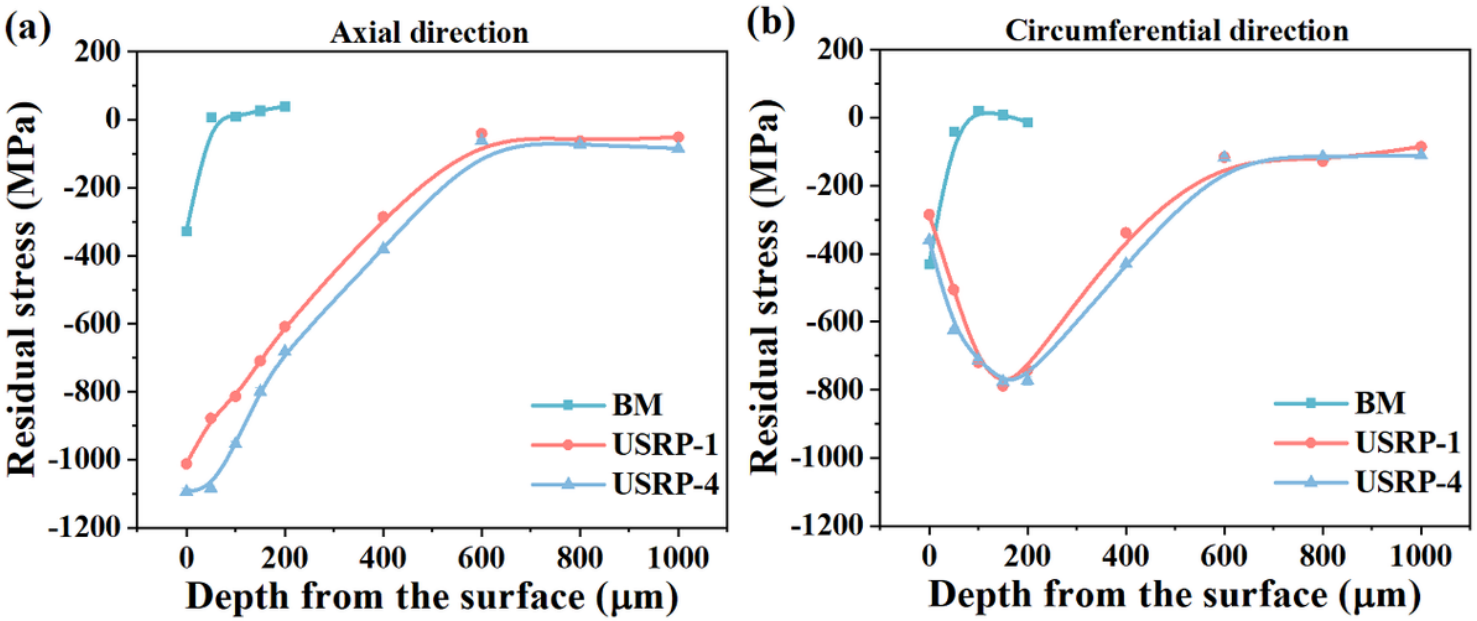

Figure 12

RS (a) along the axial direction, (b) along the circumferential direction.

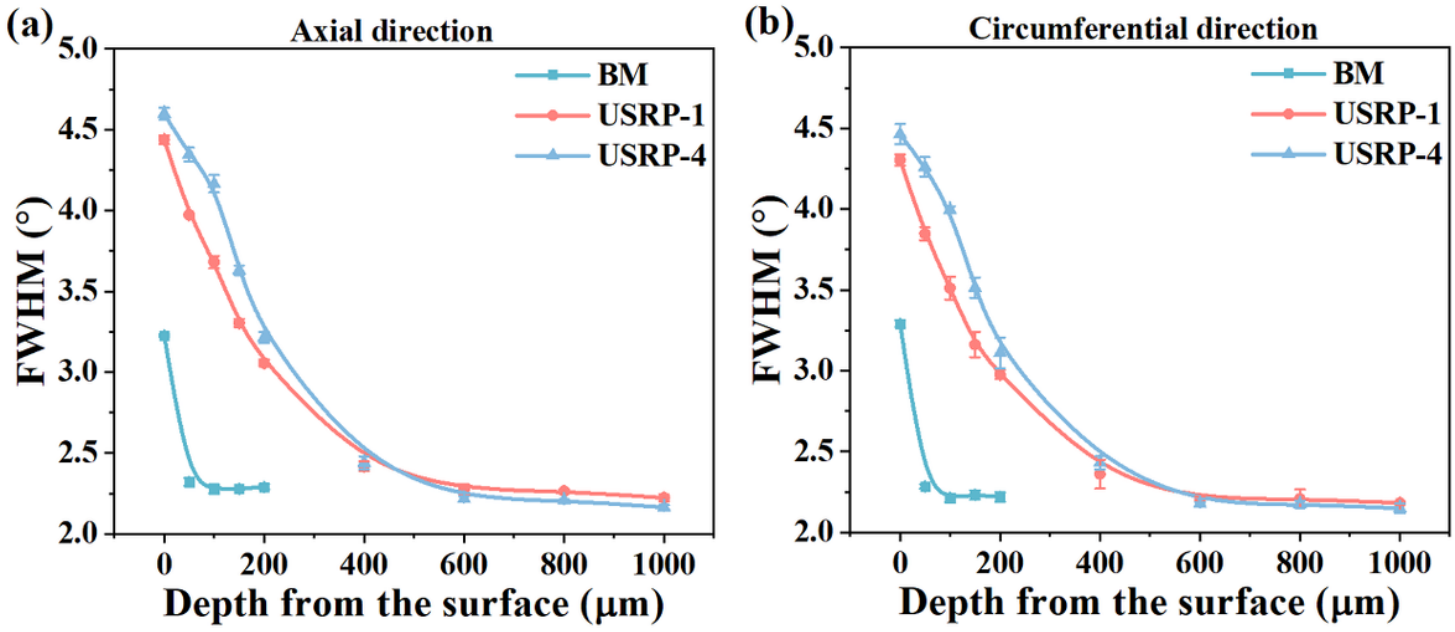

Figure 13

(a) FWHM profiles along the axial direction, (b) FWHM curve along the circumferential direction

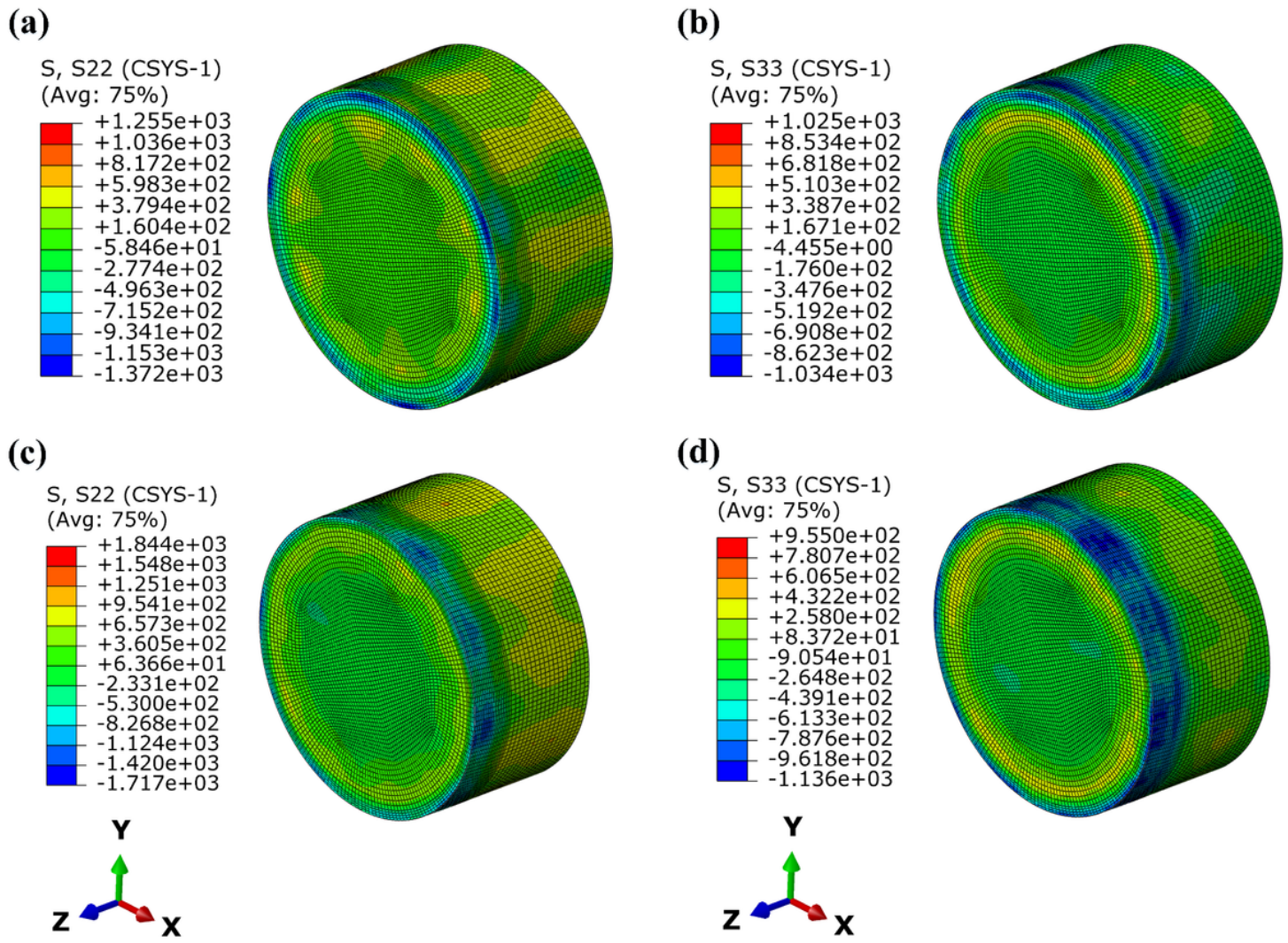

Figure 14

The stress contour plot without (a, b) USRP-1 treatment. (c, d) USRP-4 treatment.

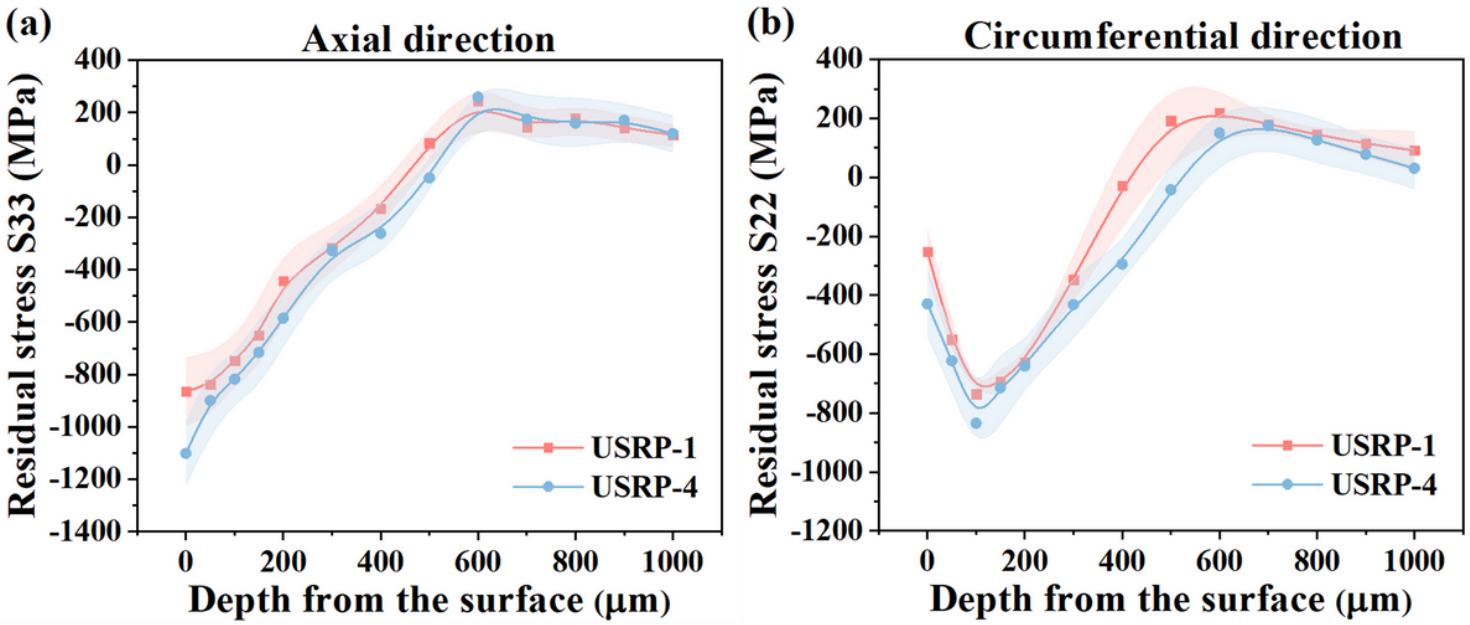

Figure 15

RS: (a) along the axial direction, (b) along the circumferential direction.

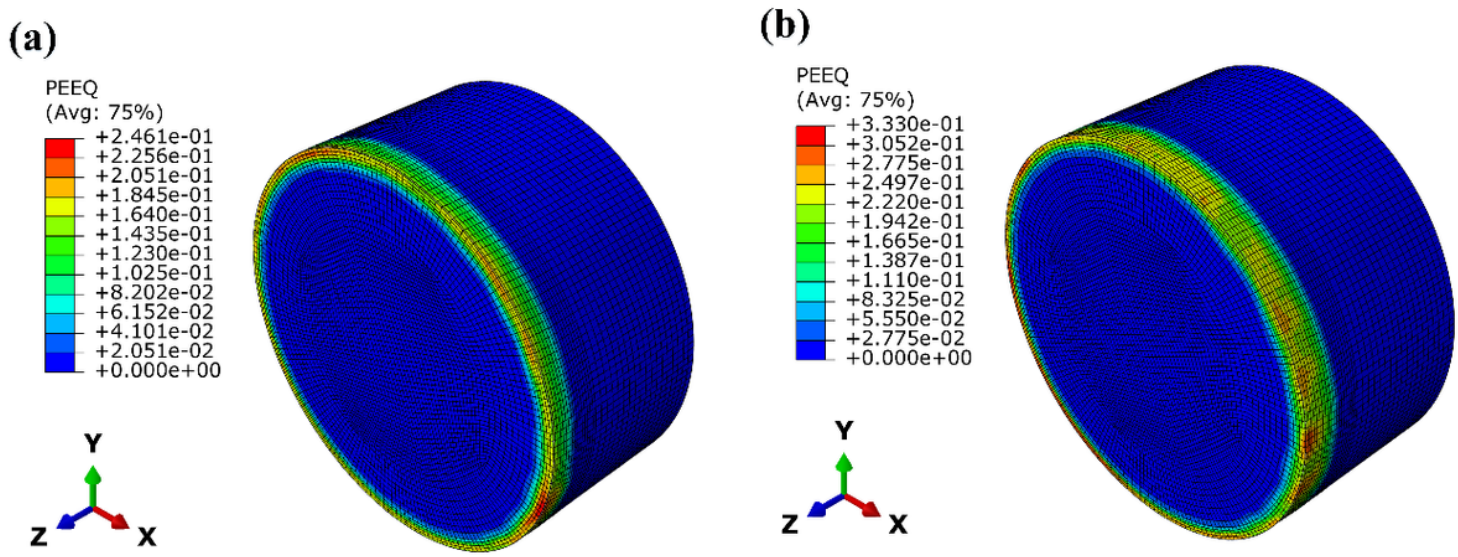

Figure 16

The equivalent plastic strain contour plot:(a) USRP-1 treatment; (b) USRP-4 treatment.

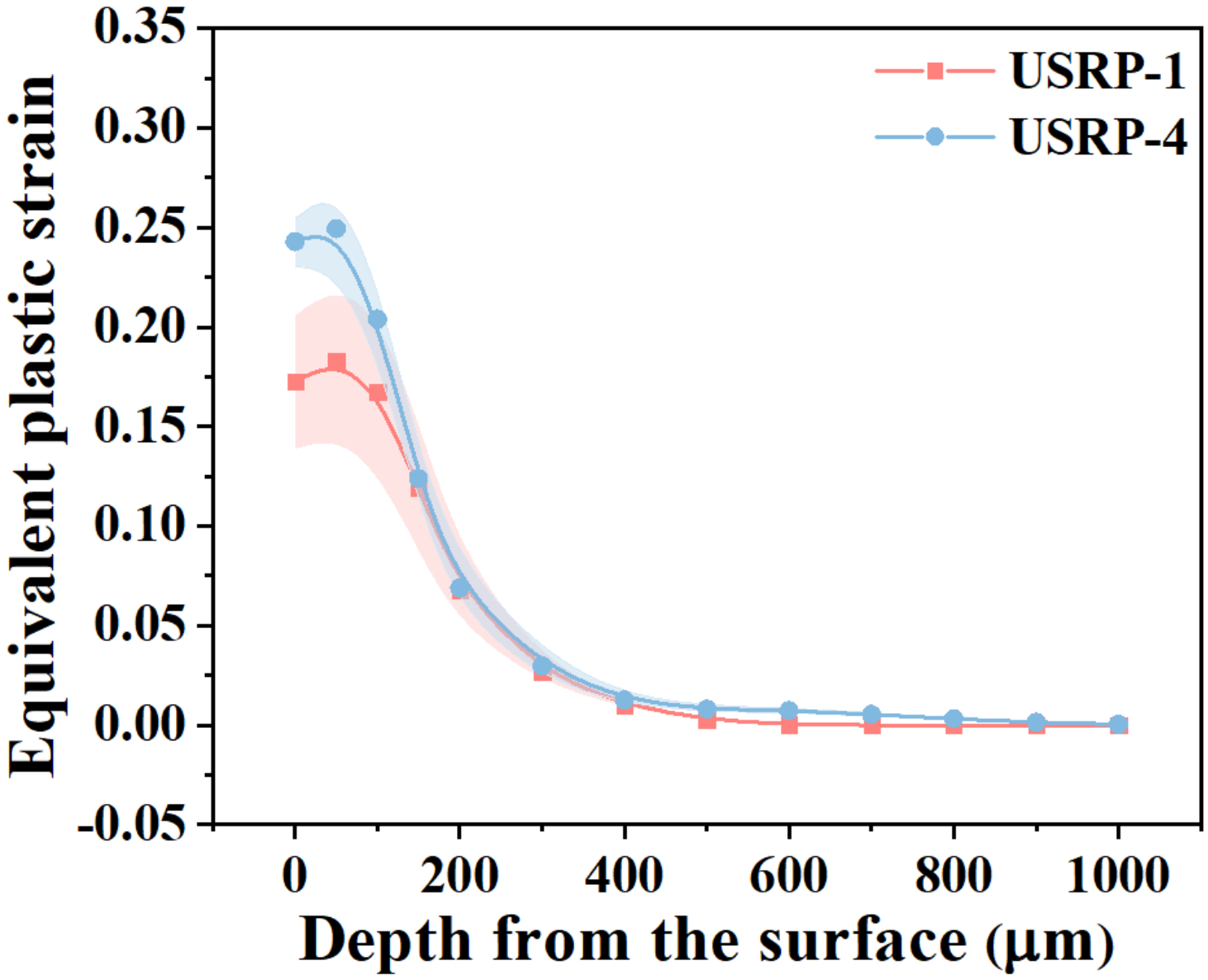

Figure 17

Equivalent plastic strain distribution.